Materials & Design 225 (2023) 111520

Contents lists available at ScienceDirect

Materials & Design

journal homepage: www.elsevier.com/locate/matdes

Microstructure and mechanical properties of aluminum-steel dissimilar metal welded using arc and friction stir hybrid welding

Ji Liu [a], Bintao Wu [b], Ziran Wang [a], Chunwang Li [a], Guangyu Chen [c], Yugang Miao [a,*]

[a] National Key Laboratory of Science and Technology on Underwater Vehicle, Harbin Engineering University, Harbin 150001, China
[b] School of Materials and New Energy, Ningxia University, Yinchuan 750400, China
[c] School of Aerospace, Transport and Manufacturing, Cranfield University, MK43 0AL, United Kingdom

HIGHLIGHTS

- A new arc and friction stir hybrid welding process was successfully developed to join aluminum to steel.
- Optimizing the BC-MIG welding process parameters could reduce the thickness of brittle intermetallic compound layer to within 1.5 μm.
- The hybrid welded joints provided superior mechanical properties with fractures in the aluminum base metal.
- The relationship between microstructure, mechanical strength and fracture mechanism was analyzed.

GRAPHICAL ABSTRACT

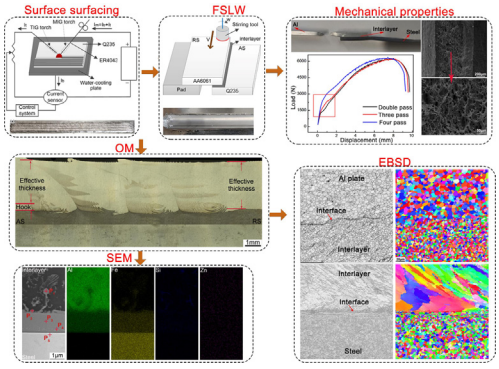

ARTICLE INFO

Article history:
Received 30 October 2022
Revised 14 December 2022
Accepted 18 December 2022
Available online 19 December 2022

Keywords:
AFSW
Aluminum-steel joint
Interfacial microstructure
Mechanical strength

ABSTRACT

In this study, arc and friction stir hybrid welding (AFSHW) was proposed to weld aluminum-steel dissimilar metals in attempt to realize high quality joining. Firstly, an interlayer was produced on galvanized steel by using bypass current-metal inert gas welding (BC-MIG), and then an aluminium plate was jointed via Friction stir lap welding (FSLW). The effects of tool pin length and FSLW times on the microstructure and mechanical properties of dissimilar joints were fully investigated by means of Optical Microscopy (OM), Scanning Electron Microscope (SEM), Electron Backscatter Diffraction (EBSD), and mechanical testing. The results show that as pin length increased, joint strength tended to increase and then decrease, and the tensile failure partially occurred at aluminium base metal. However, with additional number of FSLW, joint strength would be reduced, which was attributed to attenuated dislocation density and strain concertation in dissimilar joint. The research outcomes will provide a new welding method to obtain sound Al-Fe dissimilar metal joint, and benefit to a better understanding of Al-Fe joining mechanism.

1. Introduction

Lightweight design, energy saving and emission reduction have become the consensus of manufacturing industry [1]. Aluminum and its alloy characteristics low specific gravity, low density and high specific strength, and steel has the advantages of high strength and high creep resistance, which could be combined as a promising structure to reduce weight [2]. However, due to the difference in the thermophysical properties, it is difficult to join aluminum and steel as the brittle intermetallic compound (IMC) easily generates at the interface of two metals, thereby impeding its wide application [3]. The joining of aluminum and steel has attracted a lot of attention from both academic and industrial sectors.

* Corresponding author.
E-mail address: 18846091217@163.com (Y. Miao).

https://doi.org/10.1016/j.matdes.2022.111520
0264-1275/

To achieve a reliable connection of aluminum-steel dissimilar metals, the defects, including porosity, residual stress, crack and the thickness of IMC layer need to be controlled. As a solid-state welding method, explosive welding was known for its high ability to connect dissimilar metals [4]. Industrial production usually used transition joints prepared by explosion welding to achieve the connection of aluminum-steel dissimilar metals, but where structure thickness and production costs are increased spontaneously. Low heat input welding methods, melt-brazing using arc or laser, have also been paid a lot of attention in recent years [5]. It is found that applying the melt-brazing can effectively suppress the generation of brittle IMCs and reduce the thermal stress at the interface of dissimilar joint. For Al-Fe joints, Mathieu et al. [6] showed that when the thickness of IMC layers was controlled in around 10 μm, IMCs had almost no effect on joint strength. Mehta et al. [7] further found that the thickness of IMC layer within 2 μm helped to improve the interface strength of aluminum-steel. Zhang et al. [8] successfully jointed 1 mm aluminum plate and 1 mm galvanized steel plate by using CMT and found that the HAZ near aluminum side had inferior properties compared to interface, even the thickness of IMC layer exceeded 40 μm. Since the melt brazing joints of aluminum-steel have a dual character, with a melt part on the aluminum side and a brazing part on the steel side [9], Fe-Al melt-brazing joints require both controlling interfacial IMCs growth and avoiding HAZ softening.

Friction stir welding (FSW) can be performed at the relatively low temperature with short thermal cycles, thereby it can be used to reduce porosity, residual stress and thickness of IMC layer [10]. Ibrahim et al. [11] studied the effects of process parameters on the mechanical properties of aluminum-steel FSW joints and found that applying high welding speed and rotation speed could lead to surface void defects, high welding speed and low rotation speed could bring weaken bounding to the interface, and low welding speed and high rotation speed could produce a large amount of IMCs. Elrefaey et al. [12] indicated that when tool pin was slightly inserted into steel surface, mechanical properties of aluminum-steel joints presented a significant improvement due to the formation of a thin IMC layer. However, it is difficult to control pin depth during welding and a small difference in pin depth can cause extensive defects or IMCs [13,14]. Overall, FSW parameters exhibits only a limited range to obtain good aluminum-steel dissimilar joint without any defects. Moreover, steel material often has large hardness that will accelerate pin wear and tear, meanwhile worn-out tool materials still remain at the joint, which will affect the joint's chemical composition. Huang et al. [15] designed a pin with a circumferential notch to eliminate hook defects and reduce the wear rate of pin in FSLW. However, this method does not solve the wear problem of steel-to-pin. Zheng et al. [16] proposed a method of adding Zn foil as an interlayer to avoid direct insertion of pin into steel during aluminum-steel FSLW. However, Fe-Al joints with Zn interlayers cannot survive the high temperature on account of low melting point of Zn. Zhou et al. [13] friction surfaced an aluminum alloy interlayer on the steel surface before FSLW, and the pin was inserted into the interlayer instead of stirring steel plate to avoid pin wear, and this interface layer was recognized as an aluminum-steel diffusion layer. However, the interface strength between interlayer and steel is low due to void defects caused by friction surfacing. Zhang et al. [17] proposed a method of friction stir brazing that used a thin pure aluminum plate as a interlayer to join steel and aluminum by thermomechanical action with a large diameter shoulder without pin, which solved the problems related to FSLW (e.g. pin wear, narrow bonding area, hook defects). Unfortunately, the bonding force at the aluminum-steel interface is weaken due to insufficient heat input. The torsional fracture is prone to occur at the top of aluminum plate due to the strong torsional deformation of large diameter shoulder.

Accordingly, a novel welding method should be proposed by combining arc melt-brazing and FSW to overcome their own individual shortcomings in joining dissimilar metals. In this study, arc and friction stir hybrid welding (AFSHW) were used to realize a good connection between aluminum and steel dissimilar metals. Firstly, an aluminum interlayer was coated on the surface of substrate steel by using BC-MIG, and then aluminum plates were welded by FSLW using multi-pass path. It is expected that such a new process can fully resolve not only the problems derived from the shortcomings of porosity, thick IMC layer, narrow bonding area and heat affected zone softening in melt-brazing, but also that of pin wear, narrow process parameters, hook defects in FSLW, which cannot be addressed by other known single method. The microstructural observation, including phase composition, grain size, orientation and texture was performed on an optical microscope (OM), scanning electron microscope (SEM) and electron backscatter diffraction (EBSD), aiming at the better understanding of interface connection. Particularly, the influence of FLSW times and tool pin length on the microstructure and mechanical properties were fully explored.

2. Experiment

The experiments were conducted on AA6061 aluminum alloy plate and Q235 galvanized steel plates with a dimension of 200 mm × 80 mm × 3 mm (length × width × thickness). The chemical compositions were listed in Table 1. Zn coating could improve the wettability of liquid aluminum on steel substrate surface. The filling material was ER4043 wire with a diameter of 1.2 mm, and its chemical composition was also shown in Table 1. Si elements in wire can inhibit IMCs growth in Fe-Al joints [3].

A schematic diagram of AFSHW process was shown in Fig. 1 (a). The process was mainly divided into two steps. Firstly, an interlayer was coated on the surface of galvanized steel using BC-MIG welding. The welding parameters were listed in Table 2. Bypass current was used to reduce the heat input of base metal. The water-cooled plater was applied to improve cooling rate. As shown in Fig. 1 (b), MIG welding torch was set to 60°with substrate. TIG torch was set to 30°with substrate and perpendicular to MIG torch, which can allow large heat input to melt welding wire instead of into base metal. In addition, the bypass arc before MIG arc along the welding direction could preheat steel plate by arc heat to reduce the surface tension of liquid aluminum on the steel base metal, thus improving the wettability and spreading of liquid aluminum [18].

Secondly 6061Al alloy plate and Q235 galvanized steel with interlayer were connected by FSLW after the interlayer was milled to 1 mm thickness. FSLW was performed at the joints with differ-

Table 1
Chemical compositions of AA6061, Q235 and ER4043 (wt%).

Material	Al	Fe	Si	Cu	Mn	Mg	Zn	Cr	Ti	C	S
AA6061	Bal.	0.7	0.6	0.25	0.15	1.1	0.25	0.2	0.15	–	–
Q235	–	Bal.	0.22	–	0.48	–	–	0.19	–	0.16	≤0.045
ER4043	Bal.	0.8	5.0	0.3	0.05	0.05	0.1	–	0.2	–	–

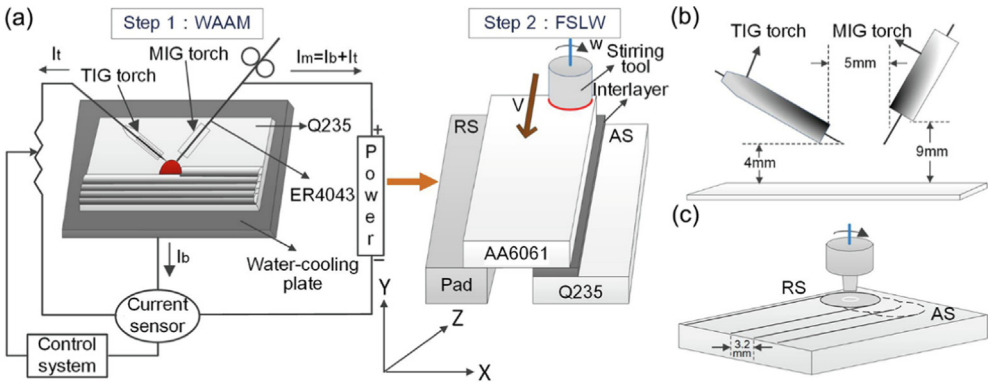

Fig. 1. Schematic diagram of (a) the AFSHW process (step 1- SS, step 2-FSLW), (b) welding torch location in the step 1, (c) the position and relationship between adjacent pass in step 2.

Table 2
Welding parameters.

Parameters	Symbol	Details
Main current	I_m	75A
Main arc voltage	–	15 V
Bypass current	I_t	25A
Welding speed	–	0.90 m/min
Flow rate of argon in the MIG torch	–	15 L/min
Flow rate of argon in the TIG torch	–	5 L/min

ent pin lengths and FSLW times. The welding parameters is shown in Table 3. As shown in Fig. 1 (c), the offset of adjacent welding pass for multi-pass FSLW process is 3.2 mm. It needs to be mentioned that the aluminum plate set on retreating side (RS) is better to joint mechanical than on advancing side (AS) in muti-pass FSLW, which will be further discussed in next section.

As shown in Fig. 2, metallographic and tensile samples were made perpendicular to the welding direction by wire cut electrical discharge machining. The macro and micro morphology of weld cross-section were observed through an optical microscope (OM, Olympus DSX 510). The interface layer was further observed by a scanning electron microscope (SEM, Zeiss-MERLIN Compact) equipped with an energy dispersive spectrometer (EDS, EDAX Octane Plus). The phases were identified by X-ray diffraction (XRD, D/max-2500X). Grain morphology and texture were observed by electron backscatter diffraction (EBSD, Oxford Instrument). The harnesses of weld at the different locations were measured by using a Vickers hardness tester (HMAS-D1000Z), with a load of 200 g in Al alloy and a load of 300 g in steel. These joints with a width of 10 mm were stretched through a universal testing machine(Instron 5967)at a rate of 3 mm/min.

3. Results and discussion

3.1. Macrostructure of weld appearance

Fig. 3 shows the weld appearance and cross-sectional morphology of as-welded specimens. As shown in Fig. 3(a), an interlayer was deposited on steel substrate and a well-formed weld with a smooth surface was obtained. However, porosity defects are found in the cross-section (Fig. 3(d)), which is attributed to high cooling

Table 3
Detailed welding parameters of FSLW.

No.	RotatingSpeed(r/min)rrrspeed(r/min)	Traversingspeed(mm/min)	Press-in amount(mm)	Tiltingangle(°)	Pinlength(mm)	FSLWTimes(pass)
S1	1000	150	0.2	2.5	3.2	1
S2					3.4	
S3					3.6	
S4					3.8	
S5					3.2	2
S6						3
S7						4

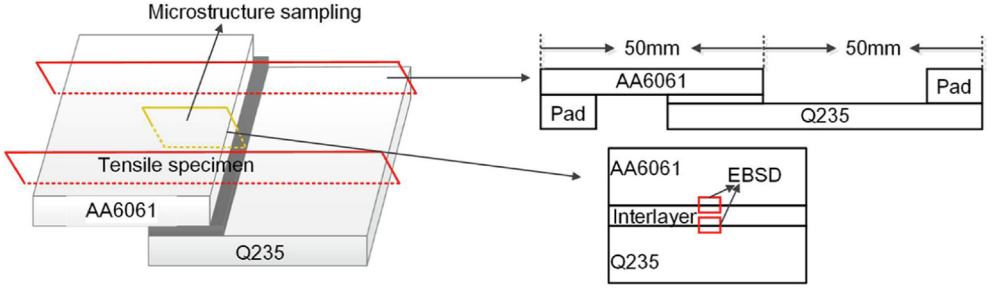

Fig. 2. The sample locations for stretching and metallography.

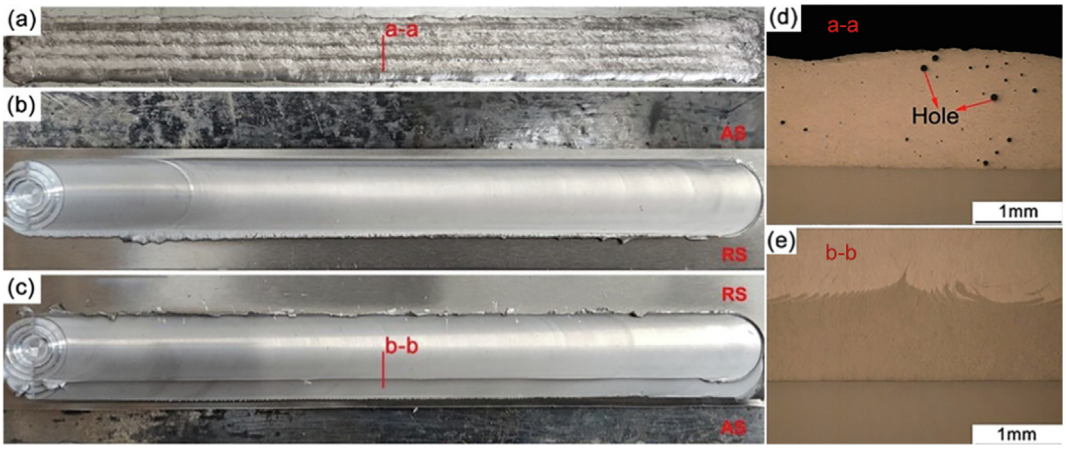

Fig. 3. The weld appearance of (a) interlayer, (b) S1 and (c) S5; the cross-section morphology of (d) a-a cross-section and (e) b-b cross-section.

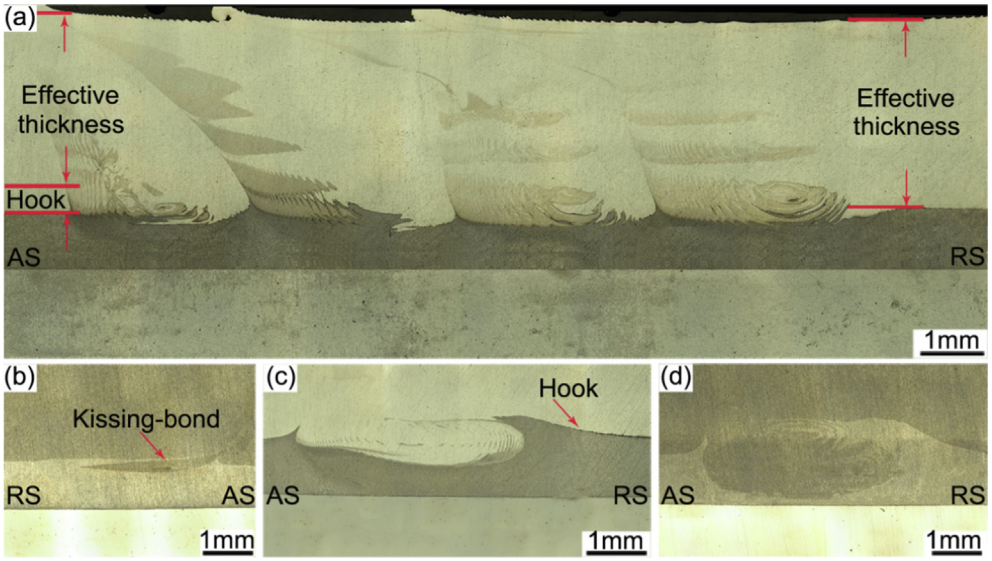

Fig. 4. The macroscopic morphology of aluminum-steel lap joints for (a) S7; (b) S1; (c) S2; (d) S4.

rate resulting in difficult escape of hydrogen pores. As shown in Fig. 3(b) and (c), the weld appearances of typical specimens for S1 and S5 are well-formed without defects such as holes, grooves and cracks. In addition, the initial porosities in interlayer can be eliminated by twisting and squeezing process from FSLW (Fig. 3 (e)).

Fig. 4 shows kissing defects and hooking defects of typical aluminum-steel lap joints for S1, S2, S4, S7. Kissing defects and hooking defects, as inherent defects in FSLW, can be clearly observed, which can reduce effective thickness for joints. When pin length is 3.2 mm, hook defects on both AS and RS are comparatively small, while there are obvious kissing defects in the stirring zone (SZ), as shown in Fig. 4(b). When pin length was increased to 3.4 mm, aluminum plate and interlayer could be fully mixed to produce a mechanical interlocking structure, while the size of hook defects would be increased, as shown in Fig. 4(c). When pin length was further increased to 3.6 mm, the kissing area and hook defect size showed a significant increase, as shown in Fig. 4(d). With FSLW times increase, kissing defects and hook defects on RS are reduced, as shown in Fig. 4(a) and (b).

The relationships between effective AS and RS thickness (ET) of joints and pin length as well as FSLW times were described in Fig. 5. The ET is primarily dependent on hook defect size. The variation in hook defect size was mainly attributed to the difference in material flow, deformation and degree of oxide film breakage during FSLW [19]. As shown in Fig. 5(a), when pin length is 3.2 mm, the material of interlayer on AS rarely flow to RS due weak mixing, resulting in slight material flow on RS in the vertical direction. Therefore, ET with 3.2 mm pin length on RS is the highest. With pin length increase, material flow in the vertical direction increases, leading to an increase in hook defects and a decrease in ET. Noteworthy, with pin length increase, a decrease in ET on RS is faster than that on AS, as more materials on AS are backfilled and stacked on RS and that cannot be fully mixed, resulting in an increase in hook defects size on RS. As shown in Fig. 5(b), FSLW times have no obvious effects on ET of AS, and the ET increases slightly on RS with FSLW times increase. Since the previous FSLW preheated the plates and broke the oxide film sufficiently, the material was well mixed without accumulating on RS in the next FSLW processes, which is consistent with Fig. 4(a).

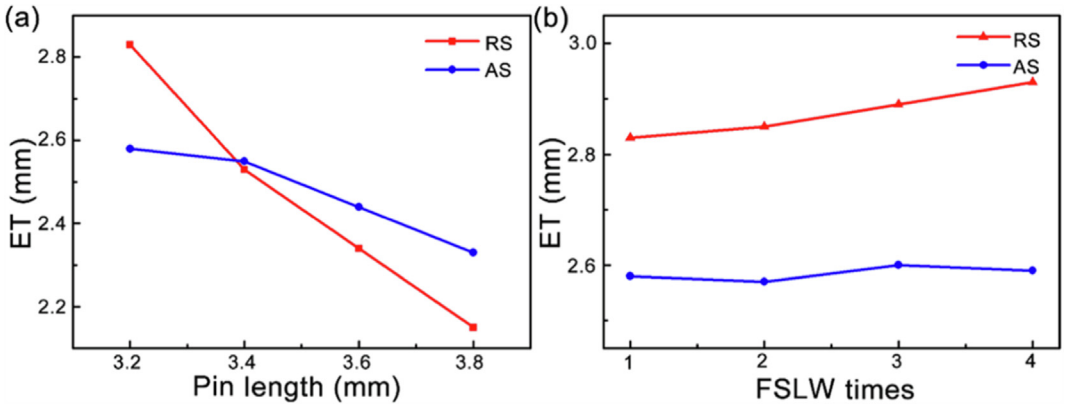

Fig. 5. The relationships between effective AS and RS thickness (ET) of joints and (a) pin length as well as (b) FSLW times.

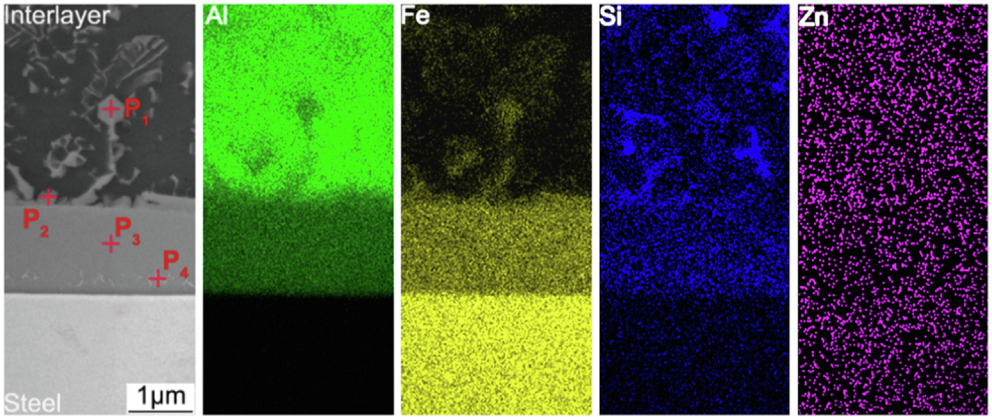

Fig. 6. HRSEM / BSE imaging and EDS mapping at the aluminum-steel interface for S1.

3.2. Microstructural evolution

The aluminum-steel interface for S1 was characterized in detail by HRSEM / BSE imaging and EDS mapping, as shown in Fig. 6. The mechanical strength of aluminum-steel joints is determined by the thickness of IMC layer [10]. As Fe and Al elements occurs diffusion along interface, a dense Fe/Al IMC layer with thickness of 1.5 μm is formed. Generally, steel material is difficult to melt, hence, Al elements are not observed on the steel side, and Fe elements are enriched in some areas on the Al side. Si element is mainly enriched near the Fe-Al IMCs to reduce the inter-diffusion rate of Al and Fe, which could enhance the interface strength [20].

Fig. 6 shows the phase composition at different locations as pitched with read crosses, and further measured data were listed in Table 4. It can be illustrated that the ratio of Fe atoms to Al atoms on points P1 and P2 is close to 1:3, which indicates the formation of FeAl3 phase. Similarly, the ratio of Fe atoms to Al atoms on points P3 and P4 are close to 2:5, which means possible Fe2Al5 phases were produced. These phases can also be evident by XRD measurement on the fractured interface between interlayer and steel, as shown in Fig. 7.

To further explore the effects of pin length and FSLW times on the IMC layer, SEM and EDS were performed on the aluminum-steel interface of S2, S4 and S7, as the results shown in Fig. 8. As shown in Fig. 8(a), when pin length is 3.4 mm, the IMC layer is a dense layer with thickness less than 1.5 μm, which is almost the same as 3.2 mm pin length. This demonstrates pin length has no effects on the thickness of IMC layer. However, as shown in Fig. 8 (b), when pin length reaches to 3.8 mm, pin will touch steel surface with 0.2 mm press-in amount of shoulder. As can be seen, a significant melting of steel surface can be observed, and the thickness of IMC layer reaches to 4.5 mm. As shown in Fig. 8(c), the thickness of dense IMC layer reaches to 2.2 μm after consecutive four-pass FSLW, indicating FSLW times have a slight effect on IMC layers. In addition, the thickness of Fe-Al diffusion layers is wider than that of dense IMCs, which may be attributed to the mutual solid solution of Fe and Al with low inter-diffusion percentage.

Table 4
Chemical composition and possible phases of the marked locations in Fig. 6.

Test points	Fe (at%)	Al (at%)	Si (at%)	Possible phase
P1	23.74	71.49	3.84	$FeAl_3$
P2	24.41	72.68	2.20	$FeAl_3$
P3	27.28	68.53	1.90	Fe_2Al_5
P4	29.16	66.59	3.06	Fe_2Al5

3.3. Grain morphology

To reveal aluminum-steel interface characteristics, taking S1 and S7 as an example, detailed description of grains was performed by using EBSD analysis. The grain morphology on the aluminum-steel interface can be divided into two parts, including Al-interlayer interface and interlayer-steel interface.

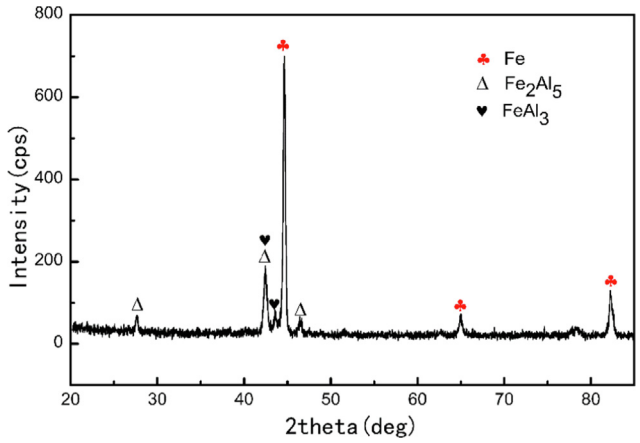

Fig. 7. XRD measurement on the fractured interface between interlayer and steel.

3.3.1. Aluminum-interlayer interface

Fig. 9 shows precipitation phases distribution and proportion of S1 and S7 in the Al-interlayer interface. Mg2Si precipitated phases are observed in the interlayer due to stirring aluminum. While precipitated phases distributed in S7 are more homogeneous than that in S1, indicating that the multi-pass FSLW helps to make a full mix of materials. From Fig. 9(c), precipitated phases proportion in S7 is 21% higher than that in S1, indicating that precipitation strengthening occurs in Al-interlayer interface with FSLW times increase.

Fig. 10 shows the EBSD pattern quality (PQ) figure, inverse pole figure (IPF) and grain size distribution in the Al-interlayer interface for S1 and S7. The PQ figure clearly illustrates the microstructure, as different grains show differences in the average pattern quality. The pattern quality of grains decreases with strain increase and shows a darker gray scale. From Fig. 10(a) and (d), the PQ figure in S7 is brighter than that in S1, indicating that grains strain in Al-interlayer decreases with FSLW times increase. Moreover, the PQ figure clearly reveals the grains and grain boundaries. S1 and

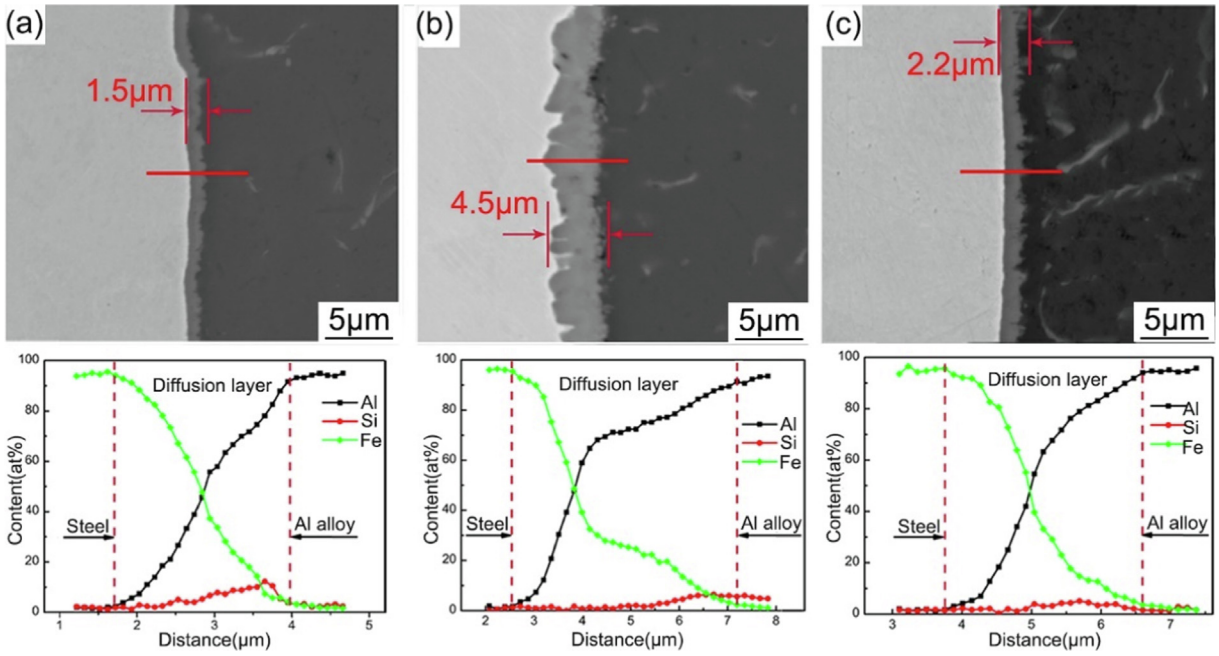

Fig. 8. SEM micrographs and EDS linear scan results on the aluminum-steel interface for (a) S2, (b) S4, (c) S7.

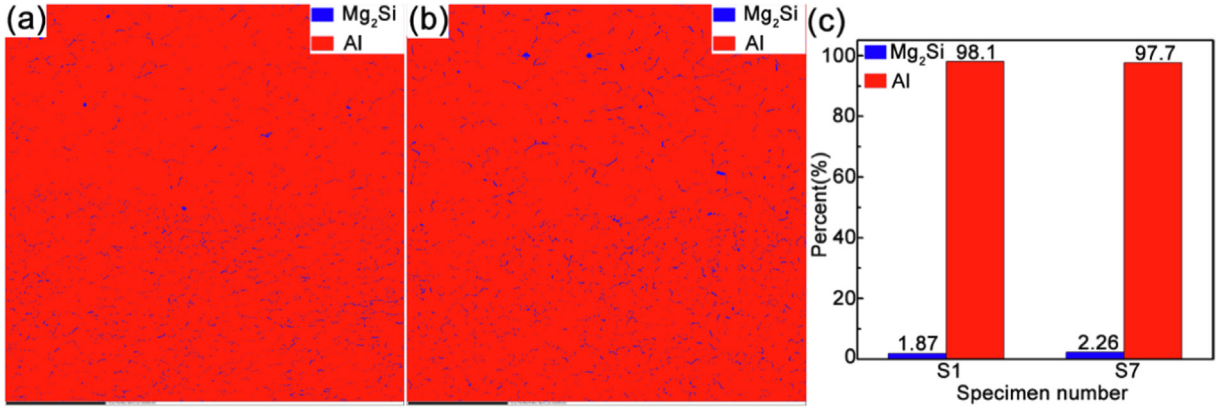

Fig. 9. The precipitation phases distribution in the Al-interlayer interface for (a) S1 and (b) S7; (c) the proportion of precipitation phases for S1 and S7.

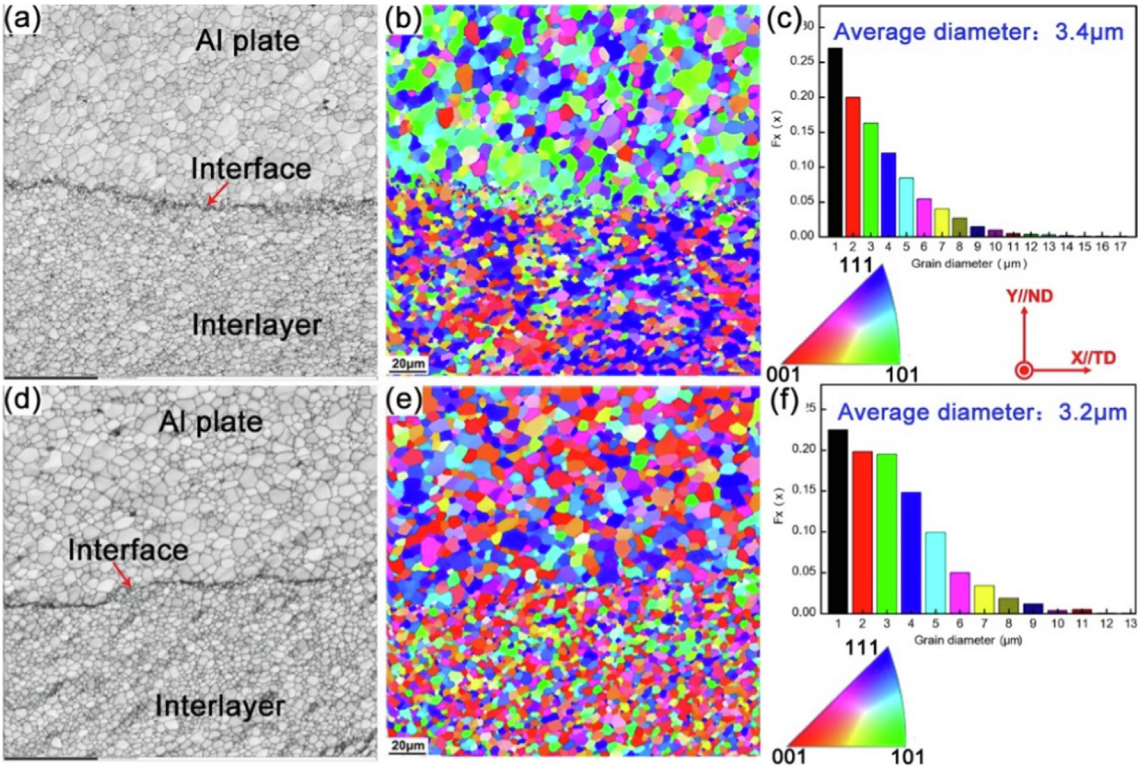

Fig. 10. EBSD scan images for S1 in the Al-interlayer interface. (a) pattern quality (PQ) figure, (b) inverse pole figure (IPF) and (c) grain size distribution; EBSD scan images for S7 in the Al-interlayer interface. (d) quality (PQ) figure, (e) inverse pole figure (IPF) and (f) grain size distribution.

S7 samples are mainly fine equiaxed grains due to dynamic recrystallization occurring in SZ. From Fig. 10(c) and (f), the grain size in S7 is slightly lower than in S1 due to higher proportion and more uniform distribution of precipitated phases in S7. A substantial proportion of precipitated phases inhibits grain boundaries motion by pinning effect, which in turn prevents the growth of recrystallized grains[21]. In addition, the grain size in Al plate is higher than that in interlayer due to precipitation phase proportion in interlayer is higher than that in Al plate (Fig. 9). From Fig. 10(b) and (e), as the same color represents the same grain orientation, the grain orientations of S1 and S7 exhibit significant inhomogeneity. The grain orientations in S1 are mainly ⟨101⟩ in Al plate, ⟨00-1⟩ and ⟨111⟩ in interlayer, which in S7 are approximately randomly distributed.

To further analyze texture, the pole diagrams in the Al-interlayer interface for S1 and S7 are shown in Fig. 11. During FSLW, the grain growth could produce meritocratic orientation under pin shear and extrusion process, resulting in directional textures. The textures of S1 and S7 are mainly composed of {112}⟨111⟩ texture. The maximum texture strength of S1 reaches to 7.1, while that of S7 decreases to 5.98. As the recrystallization ratio of S7 increased after the multi-pass FSLW, the texture strength shows a decrease.

To clarify the recrystallization mechanism, Fig. 12 shows grains characteristics distribution in the Al-interlayer interface for S1 and S7. From Fig. 12(a) and (c), grains in S1 mainly composed of recrystallized grains and subgrains, with proportions of 66.89% and 32.5%, respectively. During FSLW, grains experienced plastic deformation with tool pin and shoulder extrusion, resulting in subgrains increase, and then partial subgrains transformed into recrystallized grains in subsequent dynamic recrystallization process. With FSLW times increase, the proportion of recrystallized grains increases to 83.81% and that of subgrains decreases to 15.7%, as shown in Fig. 12(b) and (c), indicating that multi-pass FSLW can promote more subgrains into recrystallized grains.

Furthermore, from Fig. 13(a) and (c), the red line is low angle grain boundary (LAGB) from 2° to 15°, and the black line is high angle grain boundary (HAGB) over 15°. The percentage of LAGBs and HAGBs in S1 is about 35.6% and 64.4% (Fig. 13(b)), and LAGBs distribute within HAGBs. With FSLW times increase, the percentage of LAGBs and HAGBs in S7 changes to 22.8% and 77.2% (Fig. 13(e)), and partial LAGBs within grains transform into HAGBs. Therefore, it can be assumed that when subgrains were transformed into recrystallized grains, the orientation angle of LAGBs gradually increased by continuously absorbing dislocations to form HAGB, and this microstructural variation is consistent with the definition of continuous dynamic recrystallization [22,23].

GOS based on EBSD analysis are shown in Fig. 13(c) and (f). GOS figure is a favorable qualitative indicator to assess the plastic strain of material [24]. Furthermore, residual stress can be indirectly described by GOS to heterogeneous deformation of grains from high internal stress during welding [21]. From Fig. 13(c) and (f), the GOS level of S1 mainly composed of green color, while S7 is mainly described by blue color, which indicates that the deformation in S7 is lower than that in S1. Therefore, the residual stress in S7 is lower than that in S1 due to more dislocations being absorbed during continuous dynamic recrystallization.

3.3.2. interlayer-steel interface

Fig. 14 shows the EBSD pattern quality (PQ) figure, inverse pole figure (IPF) and grain size distribution figure in the interlayer-steel interface for S1 and S7. From Fig. 14(a) and (d), the PQ figure in S7 is significantly brighter than that in S1, indicating that grains strain decreases in the interlayer-steel interface with FSLW times increase. On the steel side, S1 and S7 are both fine equiaxed grains. On the interlayer side, S1 is mainly few large columnar grains and

massive fine-equiaxed grains, and the average grain diameter is 14.7 μm (Fig. 14(c)). During surface surfacing, melt pool had long dwell time due to relatively low temperature gradient and cooling rate, resulting in grain growth along the boundary towards the center of melt pool and fully developed into large columnar grains. The coarse columnar grains were twisted and squeezed during FSLW, resulting in fracture of partial grains and formation of fine equiaxed grains. With FSLW times increase, grains are continuously elongated and compressed, finer columnar grains and more equiaxed grains are formed in S7, and the average grain diameter is 11.1 μm, as shown in Fig. 14 (d) and (f). At the interface, S1 has a straight demarcation line between columnar grains of interlayer and steel, while S7 observes a darker layer of dendrites instead of demarcation line, which will improve the resistance to plastic deformation along the horizontal tensile direction. From Fig. 14(b) and (e), the grain orientations of steel in S1 and S7 are randomly distributed, and the grain orientation of interlayer in S1 is mainly ⟨101⟩, while the grain orientations of interlayer in S7 are mainly ⟨001⟩ and ⟨101⟩ .

To further analyze the texture of interlayer, the pole diagrams of interlayer in the interlayer-steel interface for S1 and S7 are shown in Fig. 15. During surface surfacing, the growth direction of epitaxial grain was close to the maximum temperature gradient direction, and the grains growth with large angle to the maximum temperature gradient direction would be suppressed, resulting in directional textures [25]. From Fig. 15(a), textures of interlayer in S1 are mainly {332} ⟨113⟩ texture with a maximum texture strength of 15. Generally, columnar grains tend to grow in the ⟨100⟩ direction along the ND compared with other growth directions due to its superior accommodation factor [26], while texture directions of interlayer changed with grain deformation due to torsion and extrusion from FSLW. From Fig. 15(b), the interlayer of S7 exhibits a multi-component texture, which is related to different directional stress caused by multi-pass FSLW, and the maximum texture strength decreases to 7.25.

Fig. 16 shows the grain boundary figure, orientation angle distribution figure and GOS figure in the interlayer-steel interface for S1 and S7. From Fig. 16(a), at the interlayer, LAGBs of S1 are

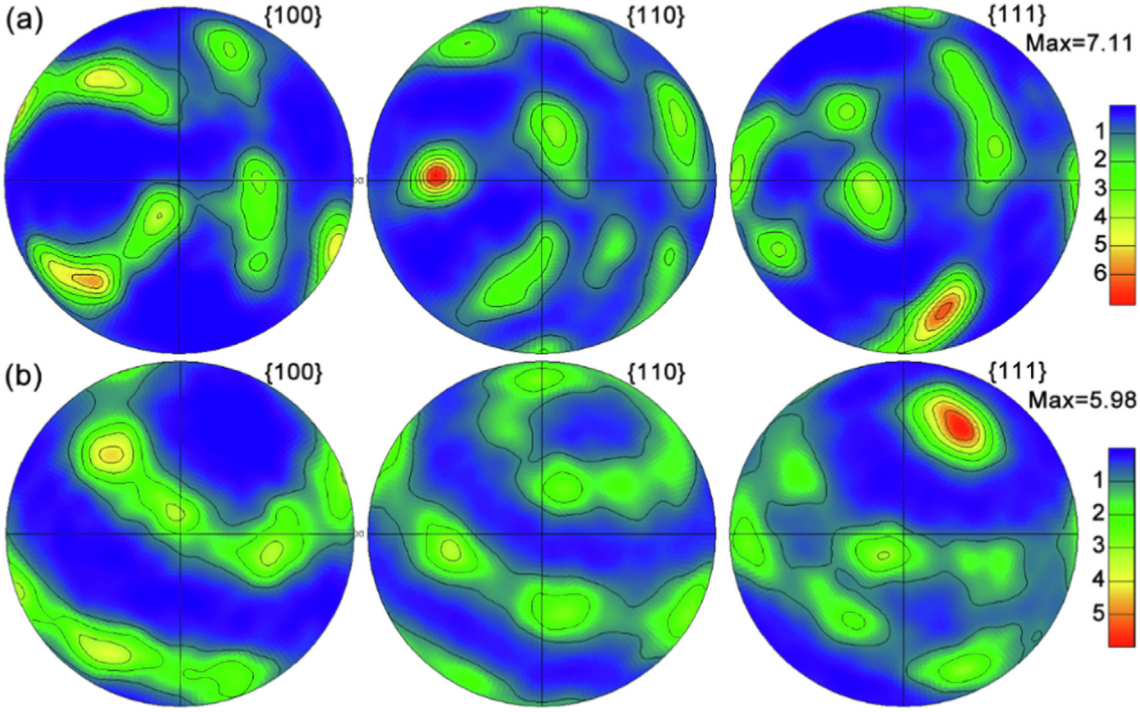

Fig. 11. The pole diagrams in the Al-interlayer interface for (a) S1 and (b) S7.

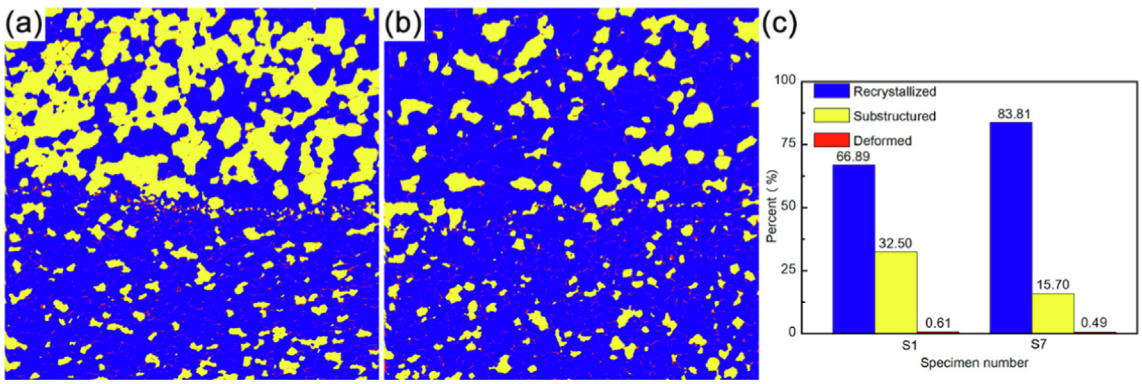

Fig. 12. The grain characteristics distribution in the Al-interlayer interface for (a) S1 and (b) S7; (c) the proportion of characteristics grains for S1 and S7.

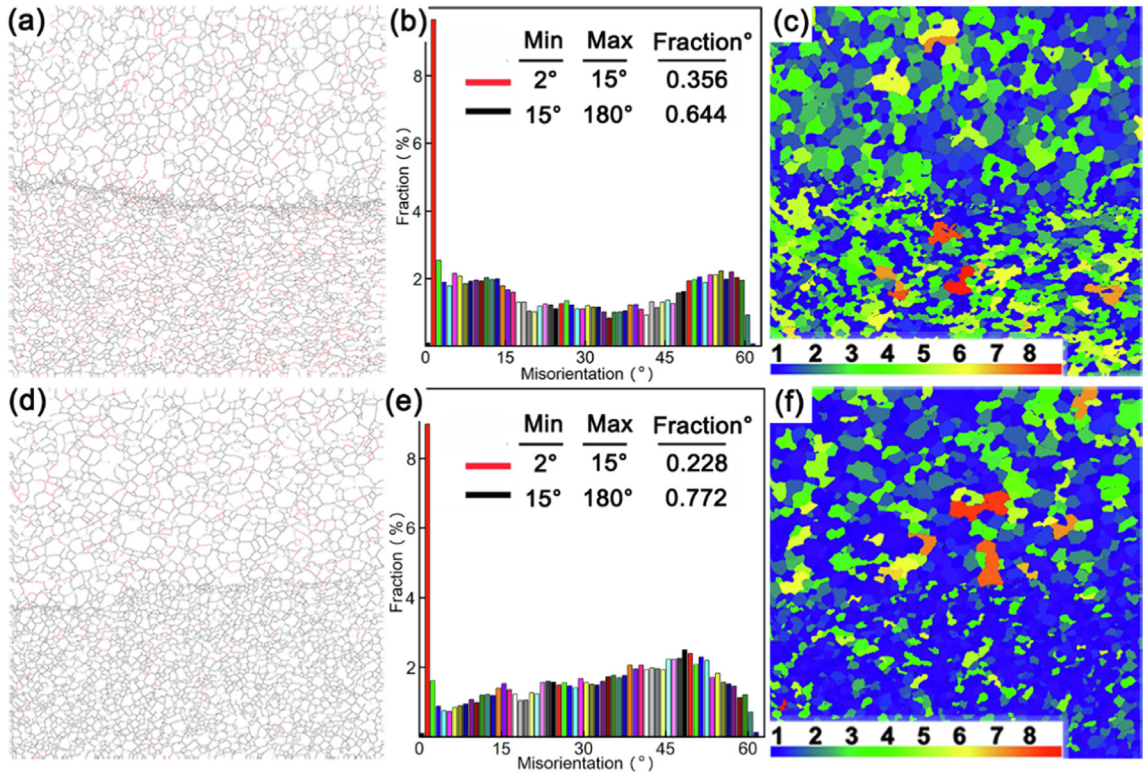

Fig. 13. The EBSD scan images of S1 in the Al-interlayer interface. (a) grain boundaries figure, (b) orientation angle distributions figure and (c) grain orientation spread figure; The EBSD scan images of S7 in the Al-interlayer interface. (d) grain boundaries figure, (e) orientation angle distributions figure and (f) grain orientation spread figure.

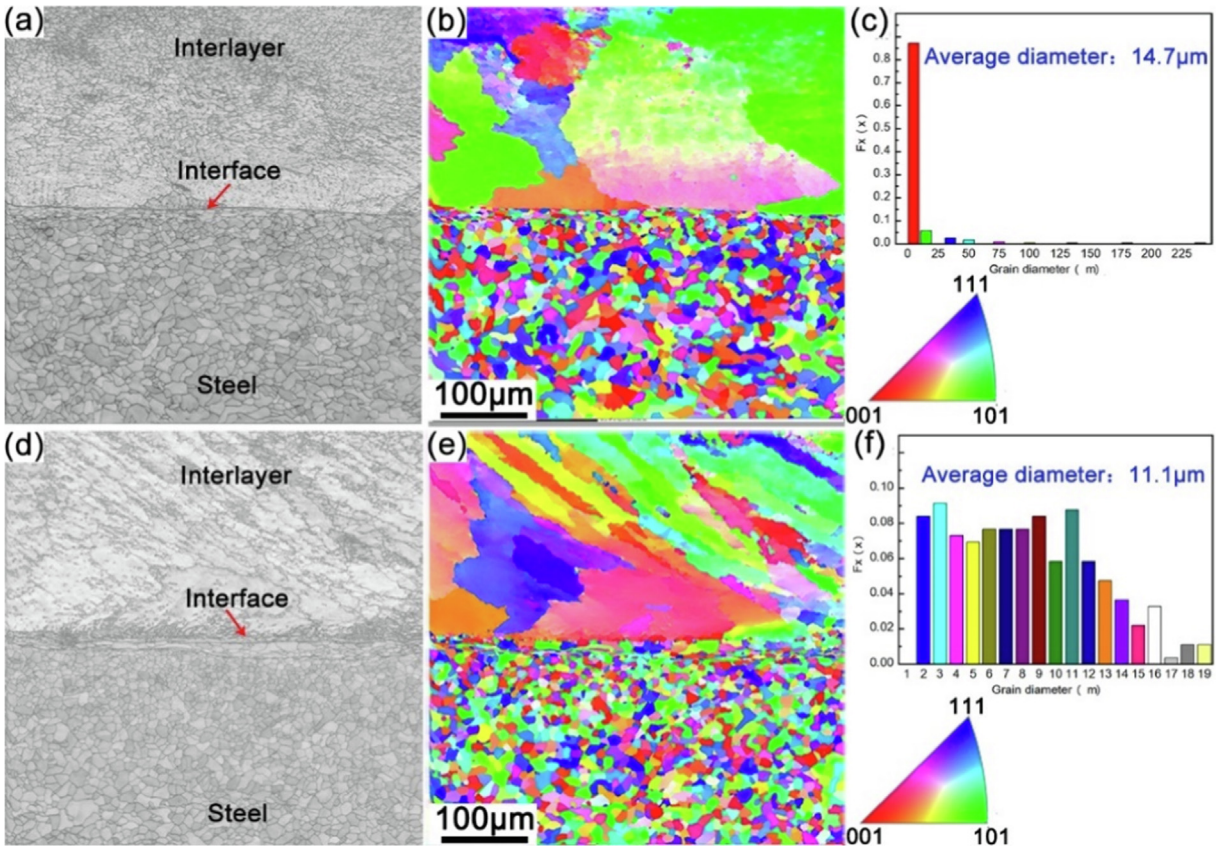

Fig. 14. EBSD scan image for S1 in the interlayer-steel interface. (a) pattern quality (PQ) figure, (b) inverse pole figure (IPF) and (c) grain size distribution; EBSD scan image for S7 in the Al-interlayer interface. (d) quality (PQ) figure, (e) inverse pole figure (IPF) and (f) grain size distribution.

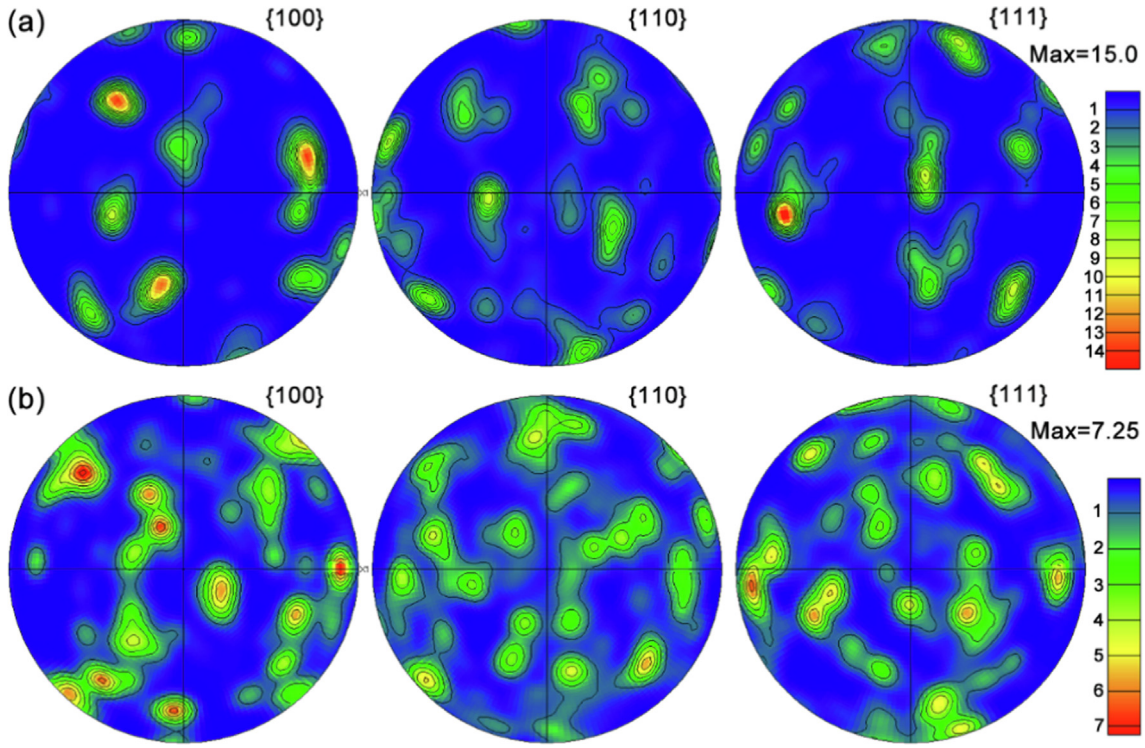

Fig. 15. The pole diagrams of interlayer in the interlayer-steel interface for (a) S1 and (b) S7.

inhomogeneously distributed inside grains or at subgrain boundaries, while HAGBs are distributed at grain boundaries, with the proportion of LAGBs reaching 89% and that of HAGBs accounting for 11%. The grain inherent dislocations produced by surface surfacing sharply increased due to torsion and extrusion from tool pin and shoulder. Moreover, friction heat promoted dislocation slip and climb, leading to the formation of massive LAGBs. With FSLW times increase, the proportion of HAGBs in S7 increases to 26.3%,

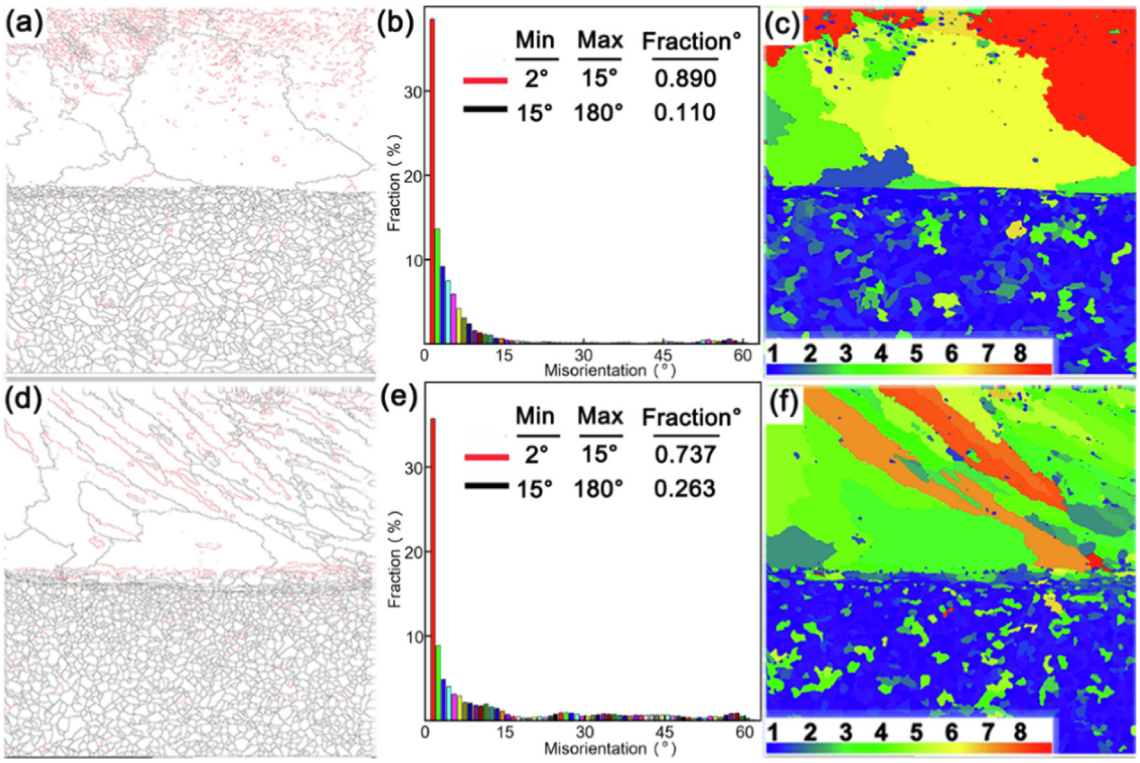

Fig. 16. EBSD scan images for S1 in the interlayer-steel interface. (a) grain boundaries figure, (b) orientation angle distributions of interlayer figure and (c) GOS figure; EBSD scan images for S7 in the interlayer-steel interface. (d) grain boundaries figure, (e) orientation angle distributions of interlayer figure and (f) GOS figure.

while the proportion of LAGBs decreases to 73.7%, which can be attributed to two reasons. On the one hand, the torsion and extrusion of muti-pass FSLW caused grains rotating and deviating from original orientation, resulting in partial LAGBs rotating to HAGBs under the action of large strain. On the other hand, as thermal cycling increased during muti-pass FSLW, partial LAGBs continuously absorbed dislocations, resulting in a gradual increase in subgrain boundary orientation angle to form HAGBs. Furthermore, the GOS levels for S1 and S7 are mainly blue on the steel side, indicating the plastic deformation and residual stress of steel is low. On the interlayer side, S1 mainly composed of yellow and red, while S7 is mainly described by green, which indicates that the deformation and residual stress of S7 are lower than that of S1. The strength of aluminum-steel lap interface is negatively correlated with the residual stress difference on both sides of aluminum-steel interface [27]. Therefore, interfacial strength in S7 is higher than that S1 due to relatively low residual stress difference on both sides of aluminum-steel interface.

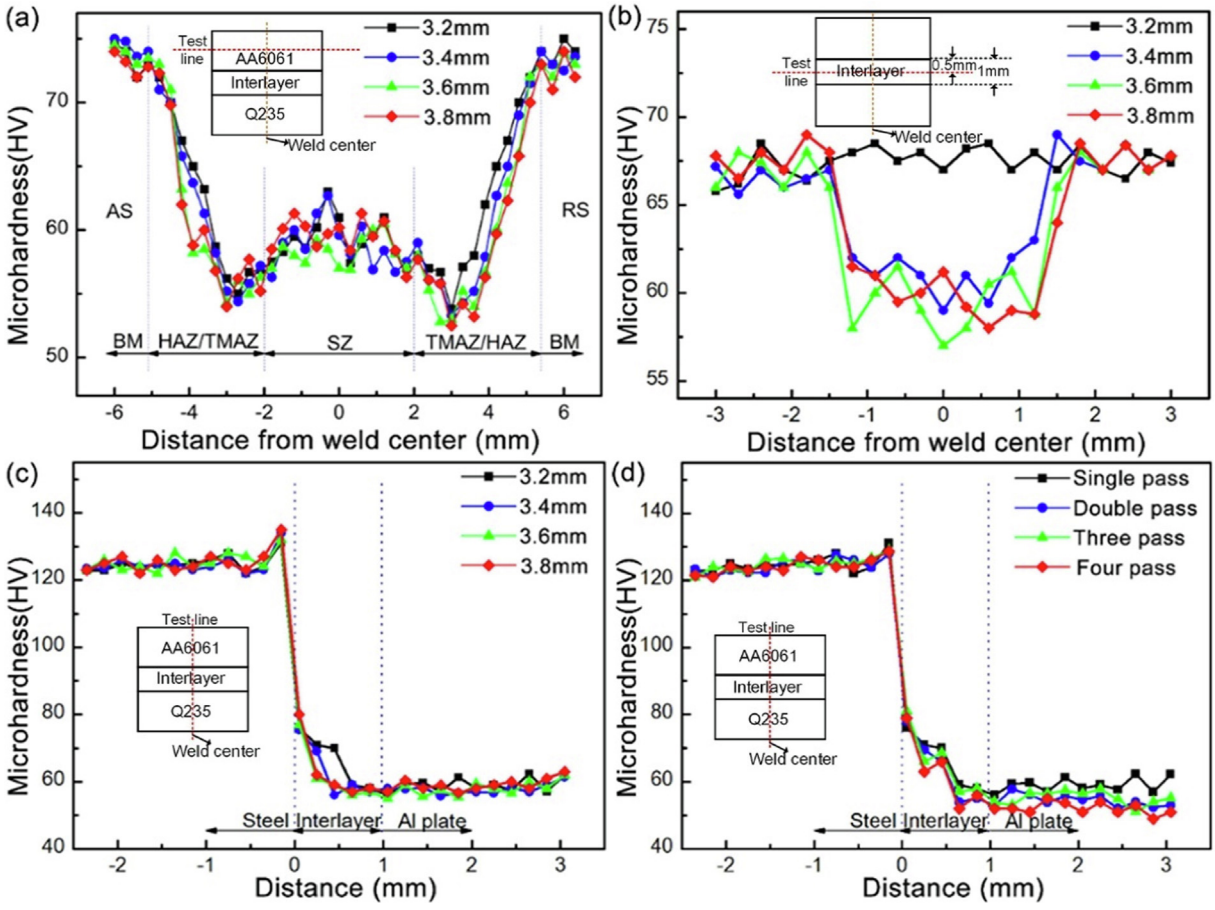

Fig. 17. The relationships in different zones between hardness distribution of joints and pin length as well as FSLW times. The hardness of (a) Al plate, (b) interlayer and (c) weld center with different pin lengths in single pass FSLW; the hardness of (d) weld center for 3.2 mm pin length with different FSLW times.

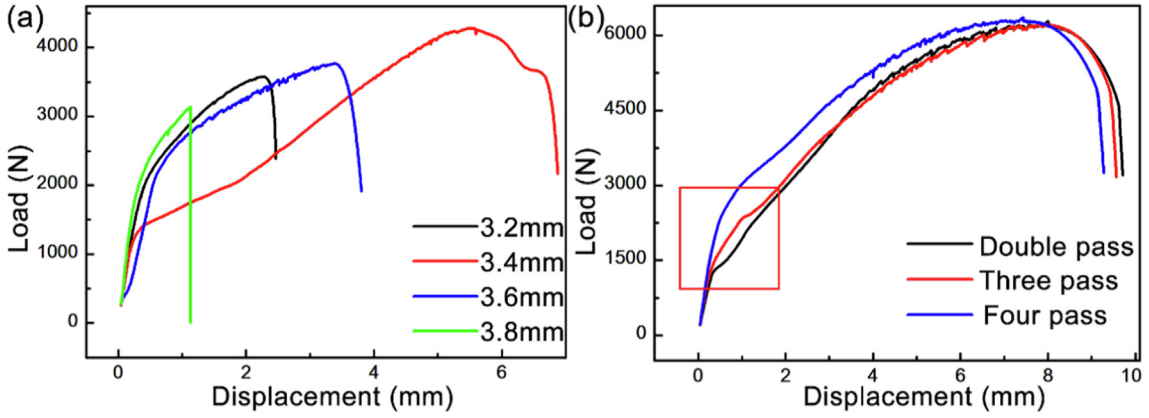

Fig. 18. The typical failure load–displacement curves for joints with (a) different pin lengths for single pass FSLW and (b) different FSLW times for 3.2 mm pin length.

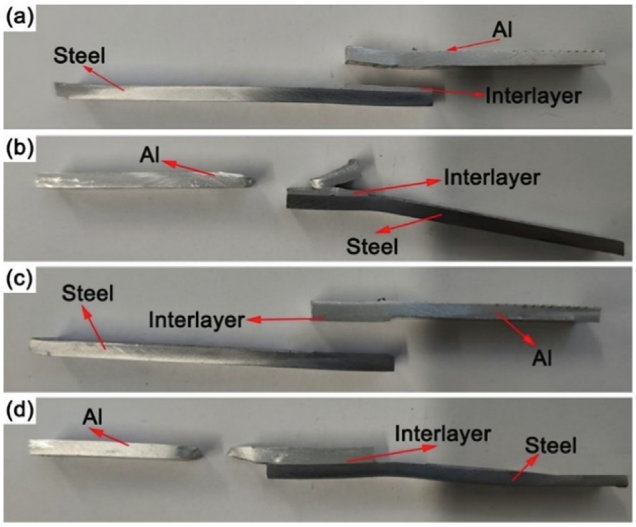

Fig. 19. The typical fracture locations of aluminum-steel joints. The fracture location (a) at the Al-interlayer interface, (b) on hook defects of RS, (c) Al-steel interface, and (d) aluminum alloy base metal.

3.4. Mechanical properties

The relationships between hardness distribution of joints and pin length as well as FSLW times were described in Fig. 17. From Fig. 17(a), the hardness distributions of aluminum plate with different pin lengths are similar and show a typical W-shape, indicating that pin length has a small effect on the hardness of aluminum plate. Fig. 17(b) shows the hardness distributions of interlayer with different pin lengths, the hardness test line with 3.2 mm pin length is all unstirred, while it contains a stirred area for other pin lengths with 0.2 mm press-in amount, and the hardness of unstirred interlayer is slightly lower than that of stirred interlayer due to high dislocation density. Fig. 17(c) shows the hardness distributions of weld center in the vertical direction, and the hardness of steel near the interface increases slightly, which is attributed to deformed grains (Fig. 14(a)). Moreover, the hardness of interlayer-steel interface is higher due to IMCs. Fig. 17(d) shows the hardness distributions along the vertical direction of weld center for different FSLW times with 3.2 mm pin length. FSLW times have almost no effect on the hardness of steel, while the hardness of interlayer and aluminum plate slightly decreases with FSLW times increase, which is attributed to a reduction in dislocation density as mentioned earlier.

Fig. 18 shows typical failure load–displacement curves for joints with different pin lengths and FSLW times, and four typical fracture locations of aluminum-steel joints are shown in Fig. 19. From Fig. 18(a), for single pass FSLW joints, when pin length is 3.2 mm, fracture occurred at the Al-interlayer interface (Fig. 19(a)) due to kissing-bond with a maximum failure load of 3,577 N. When pin length was increased to 3.4 mm and 3.6 mm, as interlocking structure was formed at the Al-interlayer interface, fracture occurred on

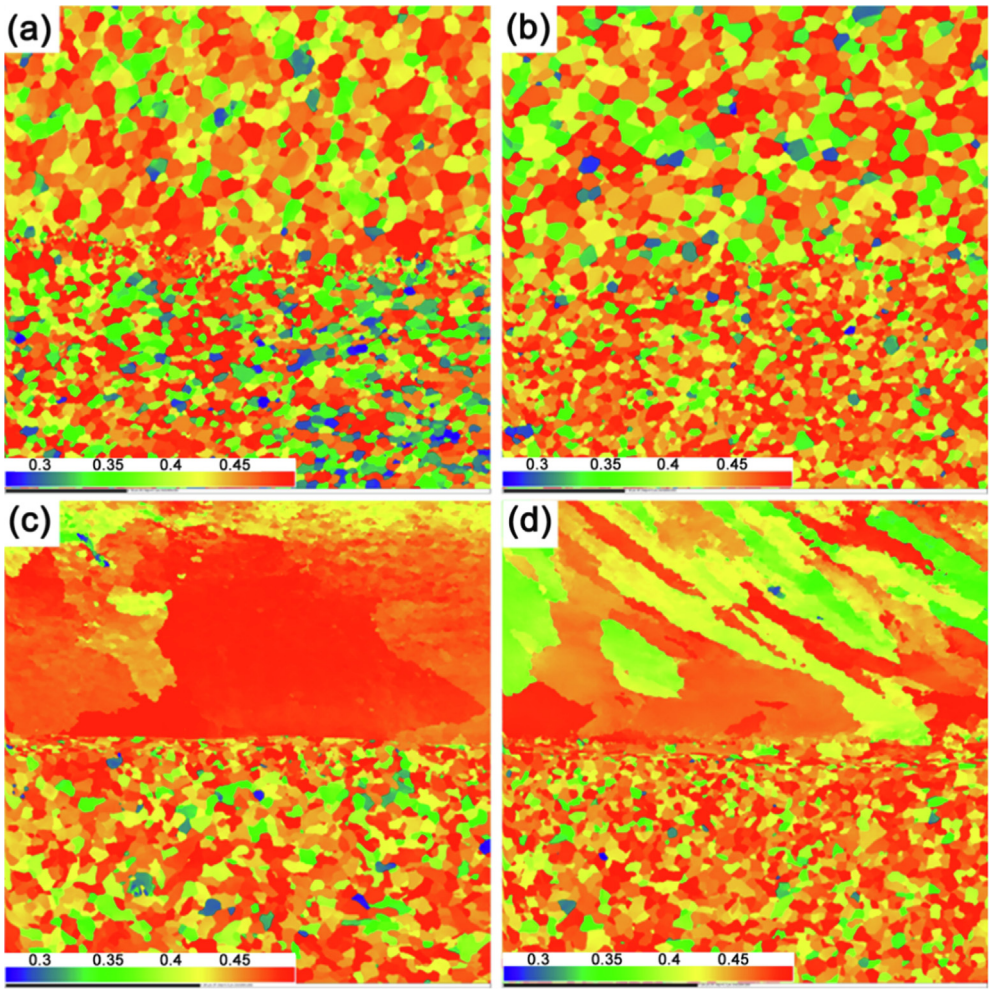

Fig. 20. The Schmid factor distribution along the tensile direction. (a) S1 and (b) S7 at the aluminum-interlayer interface; (c) S1 and (d) S7 at the interlayer-steel interface.

hook defects of RS (Fig. 19(b)) with a maximum failure load of decreasing from 4,277 N to 3,789 N, and the percentage of decrease in maximum fracture load is close to that of decrease in ET, indicating that fracture loads are determined by hook defects size. When pin length was further increased to 3.8 mm, the maximum failure load of joint was only 3,143 N with fracture occurring at the interlayer-steel interface (Fig. 19(c)) due to thick IMC layer. From Fig. 18(b), multi-pass FSLW joints with 3.2 mm pin length all fractured in the aluminum alloy base metal (Fig. 19(d)) with a maximum failure load of 6300 N, as multi-FSLW increased both Al-interlayer bonding area and joints ET. Moreover, From the red frame marked in Fig. 18(b), with FSLW times increase, the force required to open the plastic deformation of materials increases, which can be investigated by Schmid factor.

The plastic deformation of materials follows the Schmid's law [28]. When applied stress was fixed, the ease of opening sliding system depended on the Schmid factor. The larger the Schmid factor, the easier slip system opens, resulting in lower tensile strength [29]. In addition, the low Schmid factor can reduce the rate of fatigue crack expansion [30,31]. The Schmid factors for S1 and S7 along the tensile direction are shown in Fig. 20, and further measured data were listed in Table 5. The Schmid factor values of aluminum for S1 and S7 are classified with a critical value of 0.45 to divide the soft and hard orientation [29]. The percentage of softly oriented (Schmid factor over 0.45) grains in S1 and S7 are almost the same at the aluminum-interlayer interface, indicating that the resistance to plastic deformation of aluminum-interlayer is not related to FSLW times. At the interlayer-steel interface, the soft orientation grains percentage of interlayer in S1 is significantly higher than that in Al-interlayer interface and reaches 82%, and it is primarily distributed in large columnar grains (Fig. 20(c)), indicating that large columnar grains in the interlayer-steel interface first initiated plastic deformation during tension. With FSLW times increase, the percentage of softly oriented grains percentage of interlayer in S7 is slightly lower than that in Al-interlayer interface and decrease to 45%, indicating multi-pass FSLW can improve the plastic deformation resistance of joints.

Table 5
The measurement values of aluminum Schmid factor from Fig. 15 for S1 and S7.

Sample	direction	Schmid factor values	
		0.25–0.45	0.45–0.5
S1	Aluminum-interlayer	0.49	0.51
	Unstirred interlayer	0.18	0.82
S7	Aluminum-interlayer	0.5	0.5
	Unstirred interlayer	0.55	0.45

Fig. 21 shows that typical fracture surface from Fig. 19 observed by SEM to reveal the fracture mechanism. From Fig. 21(a) and (e), the fracture surfaces between Al plate and interlayer are flat in A and C regions, while the shallow dimples of different sizes are found in the B region, so it can be considered a mixed ductile–brittle fracture. From Fig. 21(b) and (f), the fracture surface on hook defects of RS consists of two parts. The dimples of D zone near hook defect are shallow and that of E zone away from the hook defect are deep due to the upward expansion of cracks along the hook defects. From Fig. 21(c) and (g), the fracture between interlayer and steel is flat without dimple, and massive IMCs are observed on the fracture surface, meanwhile load–displacement curve also show a typical brittle fracture mode. As shown in Fig. 21(d) and (h), significant necking and deep dimples are found in the fracture surface of aluminum alloy base metal, which is typical ductile fracture mode.

4. Conclusion

The current work proposed a new welding method, AFSHW, to weld aluminium and steel, and a high-quality joint was obtained. The relationships between microstructural characteristics, and mechanical strength, especially for interface regions, were fully investigated. The findings include:

(1) Compared to other process parameters, when the pin length set to be 3.2 mm, partial specimens possess the highest mechanical strength, with fracture occurring at aluminum alloy base metal. This can be attributed to the combined effects of reduced IMC layer, improved ET, enhanced bonding area and decreased residual stress.
(2) The IMC layer could be reduced to within 1.5 μm from low heat input of BC-MIG during surface surfacing. Here, it is emphasized that the low heat input from FSLW is difficult to promote IMCs growth.
(3) The short pin length could reduce the plastic flow of material in the vertical direction, and the multi-pass FSLW could promote adequate mixing of material between Al plate and interlayer due to preheating and oxide film breakage by previous FSLW, which could increase ET for dissimilar joints.

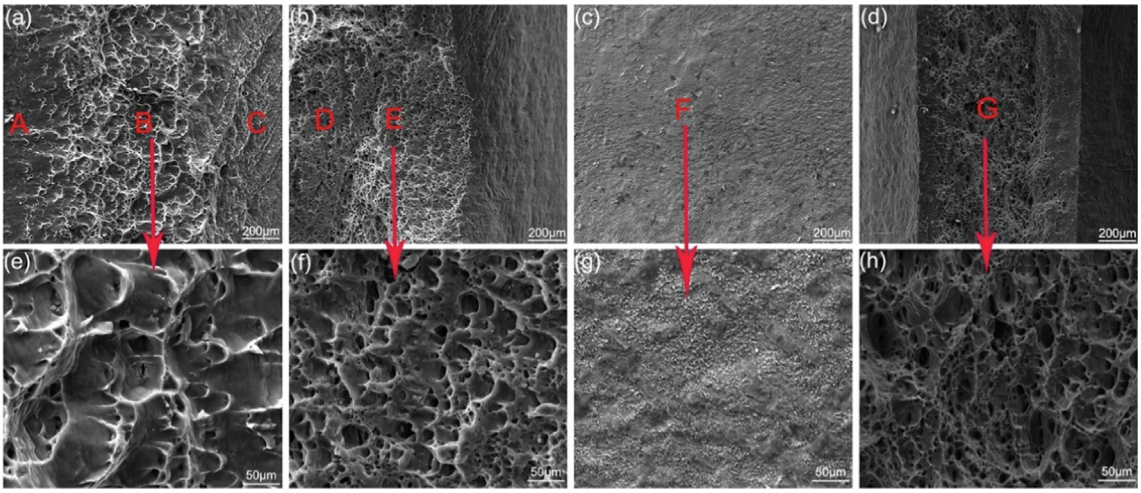

Fig. 21. The typical fracture surface from Fig. 16 observed by SEM. The SEM scanning results of fracture surface (a) at the Al-interlayer interface, (b) on hook defects of RS, (c) Al-steel interface, and (d) aluminum alloy base metal; higher magnification SEM images in (e) area B, (f) area E, (g) area F, and (h) area G.

(4) With FSLW times increase, the grains size and texture strength decreased, and the percentage of LAGBs decreased and that of HAGBs increased during continuous dynamic recrystallization. Furthermore, according to GOS and PQ, muti-pass FSLW joints showed a decrease in strain concentration and dislocation density.

Data availability

Data will be made available on request.

Declaration of Competing Interest

The authors declare that they have no known competing financial interests or personal relationships that could have appeared to influence the work reported in this paper.

Acknowledgements

The authors are greatly indebted to the State Key Laboratory of Science and Technology on Underwater Vehicle for the support on this research and the State Key Laboratory of Advanced Welding Production Technology for the tests and analyses conducted in this research. This work was supported by the National Nature Science Foundation of China [grant numbers 51975138]; the High-Tech ship Scientific Research Project from the Ministry of Industry and Information Technology ([2019]360).

References

[1] M. Li, W. Tao, J. Zhang, Y. Wang, S. Yang, Hybrid resistance-laser spot welding of aluminum to steel dissimilar materials: Microstructure and mechanical properties, Mater. Des. 221 (2022), https://doi.org/10.1016/j.matdes.2022.111022 111022.
[2] L. Wan, Y. Huang, Friction stir welding of dissimilar aluminum alloys and steels: a review, Int. J. Adv. Manuf. Technol. 99 (2018) 1781–1811, https://doi.org/10.1007/s00170-018-2601-x.
[3] K.T. Suzuki, S. Omura, S. Tokita, Y.S. Sato, Y. Tatsumi, Drastic Improvement in Dissimilar Aluminum-to-Steel Joint Strength by Combining Positive Roles of Silicon and Nickel Additions, SSRN Electron. J. 225 (2022), https://doi.org/10.2139/ssrn.4157173 111444.
[4] X. Wu, C. Shi, Z. Fang, S. Lin, Z. Sun, Comparative study on welding energy and Interface characteristics of titanium-aluminum explosive composites with and without interlayer, Mater. Des. 197 (2021), https://doi.org/10.1016/j.matdes.2020.109279 109279.
[5] C. Yuce, F. Karpat, N. Yavuz, O. Dogan, A review on advanced joining techniques of multi material part manufacturing for automotive industry, (n.d.).
[6] A. Mathieu, S. Matteï, A. Deschamps, B. Martin, D. Grevey, Temperature control in laser brazing of a steel/aluminium assembly using thermographic measurements, NDT E Int. 39 (2006) 272–276, https://doi.org/10.1016/j.ndteint.2005.08.005.
[7] K.P. Mehta, A review on friction-based joining of dissimilar aluminum-steel joints, J. Mater. Res. 34 (1) (2019) 78–96.
[8] H.T. Zhang, J.C. Feng, P. He, H. Hackl, Interfacial microstructure and mechanical properties of aluminium-zinc-coated steel joints made by a modified metal inert gas welding-brazing process, Mater. Charact. 58 (2007) 588–592, https://doi.org/10.1016/j.matchar.2006.07.008.
[9] S. Lin, J. Song, G. Ma, C. Yang, Dissimilar metals TIG welding-brazing of aluminum alloy to galvanized steel, Front. Mater. Sci. China. 3 (2009) 78–83, https://doi.org/10.1007/s11706-009-0007-2.
[10] T. Matsuda, T. Ogaki, K. Hayashi, C. Iwamoto, T. Nozawa, M. Ohata, A. Hirose, Fracture dominant in friction stir spot welded joint between 6061 aluminum alloy and galvannealed steel based on microscale tensile testing, Mater. Des. 213 (2022), https://doi.org/10.1016/j.matdes.2021.110344 110344.
[11] B.F. Batistão, L.A. Bergmann, P. Gargarella, N.G. de Alcântara, J.F. dos Santos, B. Klusemann, Characterization of dissimilar friction stir welded lap joints of AA5083 and GL D36 steel, J. Mater. Res. Technol. 9 (2020) 15132–15142, https://doi.org/10.1016/j.jmrt.2020.10.078.
[12] A. Elrefaey, M. Gouda, M. Takahashi, K. Ikeuchi, Characterization of aluminum/steel lap joint by friction stir welding, J. Mater. Eng. Perform. 14 (2005) 10–17, https://doi.org/10.1361/10599490522310.
[13] L. Zhou, M. Yu, B. Liu, Z. Zhang, S. Liu, X. Song, H. Zhao, Microstructure and mechanical properties of Al/steel dissimilar welds fabricated by friction surfacing assisted friction stir lap welding, J. Mater. Res. Technol. 9 (2020) 212–221, https://doi.org/10.1016/j.jmrt.2019.10.046.
[14] N.Z. Khan, A.N. Siddiquee, Z.A. Khan, S.K. Shihab, Investigations on tunneling and kissing bond defects in FSW joints for dissimilar aluminum alloys, J. Alloys Compd. 648 (2015) 360–367, https://doi.org/10.1016/j.jallcom.2015.06.246.
[15] Y. Huang, L. Wan, X. Meng, Y. Xie, Z. Lv, L. Zhou, Probe shape design for eliminating the defects of friction stir lap welded dissimilar materials, J. Manuf. Process. 35 (2018) 420–427, https://doi.org/10.1016/j.jmapro.2018.08.026.
[16] Q. Zheng, X. Feng, Y. Shen, G. Huang, P. Zhao, Dissimilar friction stir welding of 6061 Al to 316 stainless steel using Zn as a filler metal, J. Alloys Compd. 686 (2016) 693–701, https://doi.org/10.1016/j.jallcom.2016.06.092.
[17] G. Zhang, X. Yang, D. Zhu, L. Zhang, Cladding thick Al plate onto strong steel substrate using a novel process of multilayer-friction stir brazing (ML-FSB), Mater. Des. 185 (2020), https://doi.org/10.1016/j.matdes.2019.108232 108232.
[18] Y. Miao, Z. Ma, X. Yang, J. Liu, D. Han, Experimental study on microstructure and mechanical properties of AA6061/Ti-6Al-4V joints made by bypass-current MIG welding-brazing, J. Mater. Process. Technol. 260 (2018) 104–111, https://doi.org/10.1016/j.jmatprotec.2018.05.019.
[19] H. Chen, L. Fu, P. Liang, F. Liu, Defect features, texture and mechanical properties of friction stir welded lap joints of 2A97 Al-Li alloy thin sheets, Mater. Charact. 125 (2017) 160–173, https://doi.org/10.1016/j.matchar.2017.01.038.
[20] H. Xia, X. Zhao, C. Tan, B. Chen, X. Song, L. Li, Effect of Si content on the interfacial reactions in laser welded-brazed Al/steel dissimilar butted joint, J. Mater. Process. Technol. 258 (2018) 9–21, https://doi.org/10.1016/j.jmatprotec.2018.03.010.
[21] M.K. Alam, M. Mehdi, R.J. Urbanic, A. Edrisy, Electron Backscatter Diffraction (EBSD) analysis of laser-cladded AISI 420 martensitic stainless steel, Mater. Charact. 161 (2020), https://doi.org/10.1016/j.matchar.2020.110138 110138.
[22] S. Gourdet, F. Montheillet, A model of continuous dynamic recrystallization, Acta Mater. 51 (2003) 2685–2699, https://doi.org/10.1016/S1359-6454(03)00078-8.
[23] T. Sakai, A. Belyakov, R. Kaibyshev, H. Miura, J.J. Jonas, Dynamic and post-dynamic recrystallization under hot, cold and severe plastic deformation conditions, Prog. Mater. Sci. 60 (2014) 130–207, https://doi.org/10.1016/j.pmatsci.2013.09.002.
[24] R.R. Shen, P. Efsing, Overcoming the drawbacks of plastic strain estimation based on KAM, Ultramicroscopy. 184 (2018) 156–163, https://doi.org/10.1016/j.ultramic.2017.08.013.
[25] J. Liu, A.C. To, Quantitative texture prediction of epitaxial columnar grains in additive manufacturing using selective laser melting, Addit. Manuf. 16 (2017) 58–64, https://doi.org/10.1016/j.addma.2017.05.005.
[26] Q. Yan, B. Song, Y. Shi, Comparative study of performance comparison of AlSi10Mg alloy prepared by selective laser melting and casting, J. Mater. Sci. Technol. 41 (2020) 199–208, https://doi.org/10.1016/j.jmst.2019.08.049.
[27] G. Qin, Y. Su, X. Meng, B. Fu, Numerical simulation on MIG arc brazing-fusion welding of aluminum alloy to galvanized steel plate, Int. J. Adv. Manuf. Technol. (2015), https://doi.org/10.1007/s00170-014-6529-5.
[28] I.L. Dillamore, Plasticity of Crystals with Special Reference to Metals, Phys. Bull. 20 (3) (1969).
[29] D.E. Laughlin, K. Hono, Physical metallurgy, Newnes, 2014.
[30] M. Ma, B. Wang, H. Liu, D. Yi, F. Shen, T. Zhai, Investigation of fatigue crack propagation behavior of 5083 aluminum alloy under various stress ratios: Role of grain boundary and Schmid factor, Mater. Sci. Eng. A. 773 (2020), https://doi.org/10.1016/j.msea.2019.138871 138871.
[31] G. Sun, C. Wang, X. Wei, D. Shang, S. Chen, Study on small fatigue crack initiation and growth for friction stir welded joints, Mater. Sci. Eng. A. 739 (2019) 71–85, https://doi.org/10.1016/j.msea.2018.10.002.